



PCCP

Development of Interatomic Potential for Al-Tb Alloy by Deep Neural Network Learning Method

Journal:	<i>Physical Chemistry Chemical Physics</i>
Manuscript ID	CP-ART-03-2020-001689.R1
Article Type:	Paper
Date Submitted by the Author:	22-Jun-2020
Complete List of Authors:	Tang, Ling; Zhejiang University of Technology, Department of Applied Physics, College of Science Yang, Ze-Jin; School of Science, Zhejiang University of Technology, Wen, Tongqi; Northwestern Polytechnical University, Department of Applied Physics; Ames Laboratory Ho, Kai Ming; Ames Laboratory-U.S. DOE, Physics and Astronomy Kramer, Matthew; Ames Laboratory, Materials Science Division; Iowa State University, Materials Science and Engineering Wang, Cai Zhuang; Ames Laboratory-U.S. DOE, Physics and Astronomy

SCHOLARONE™
Manuscripts

Development of Interatomic Potential for Al-Tb Alloy by Deep Neural Network Learning Method

L. Tang¹, Z. J. Yang^{1,*}, T. Q. Wen², K. M. Ho^{2,3}, M. J. Kramer² and C. Z. Wang^{2,3,†}

¹*Department of Applied Physics, College of Science, Zhejiang University of Technology, Hangzhou, 310023, China*

²*Ames Laboratory-USDOE, Iowa State University, Ames, Iowa 50011, USA*

³*Department of Physics and Astronomy, Iowa State University, Ames, Iowa 50011, USA*

Corresponding author: * zejinyang@zjut.edu.cn † wangcz@ameslab.gov

Abstract

An interatomic potential for Al-Tb alloy around the composition of Al₉₀Tb₁₀ was developed using the deep neural network (DNN) learning method. The atomic configurations and the corresponding total potential energies and forces on each atom obtained from *ab initio* molecular dynamics (AIMD) simulations are collected to train a DNN model to construct the interatomic potential for Al-Tb alloy. We show the obtained DNN model can well reproduce the energies and forces calculated by AIMD. Molecular dynamics (MD) simulations using the DNN interatomic potential also accurately describe the structural properties of Al₉₀Tb₁₀ liquid, such as the partial pair correlation functions (PPCFs) and the bond angle distributions, in comparison with the results from AIMD. Furthermore, the developed DNN interatomic potential predicts the formation energies of crystalline phases of Al-Tb system with the accuracy comparable to *ab initio* calculations. The structure factors of Al₉₀Tb₁₀ metallic liquid and glass obtained by MD simulation using the developed DNN interatomic potential are also in good agreement with the experimental X-ray diffraction data. The development of short-range order (SRO) in Al₉₀Tb₁₀ liquid and undercooled liquid is

also analyzed and three dominant SROs, i.e., Al-centered distorted icosahedron (DISICO), Tb-centered '3661' and '15551' clusters, respectively, are identified.

I. Introduction

Aluminum-rare-earth (Al-RE) binary alloys with Al-rich composition (about 90 at. % Al) can form metallic glasses by rapid quenching from the liquid state [1]. It has been shown that these Al-RE alloys have very high strength-to-weight ratio owing to a high proportion of light weight Al [2-4]. However, Al-RE alloys belong to marginal glass-forming systems which usually have high density of nanocrystals in the samples prepared by rapid solidification process [1, 5]. Moreover, the stable as well as metastable Al-rich intermetallics vary across lanthanide series [1, 6-8].

In order to understand the microscopic mechanisms of phase formation and competition in these complex alloys, the knowledge of short to medium range structural orders in liquid and undercooled liquid at atomistic level and the corresponding time evolution of the atomistic structures during solidification/devitrification are critical. Investigation of the atomistic structural difference among these binary alloys at liquid, glass as well as crystalline phases will provide us valuable insights to further tune these alloys for better properties and glass-forming ability.

We note that while most interest in the literature has been focused on light RE (e.g., Al-Ce [8]), Al alloyed with heavy RE have not been extensively investigated, except for Al-Sm system at the composition around Al-90 at. % where both experimental studies and MD simulations using an empirical interatomic potential have been reported

[9-11]. One of the bottlenecks hindering computational simulation of Al-RE alloys is that reliable interatomic potentials for the most of Al-RE alloys (e.g., Al-Tb) are still lacking. Although *ab initio* calculations can offer high accuracy of interatomic interactions for Al-RE alloys, it can deal with only up to several hundred atoms and within a few hundred picoseconds (ps) simulation time in most of the simulations due to the expensive computational cost of the method. Therefore, it is difficult for AIMD simulations to investigate the long-time relaxation in glass and phase competition during solidification, which is a key to understand the metallic glass formation.

Machine learning potential for condensed-matter was first proposed by Behler and Parrinello [12]. After that, many other machine learning potentials were developed and applied in MD simulations [13-17]. Based on these earlier works, a deep learning method [18-20] with DNN model for many-body interatomic interactions has been developed recently which is very promising for overcoming the dilemma in simulation speed and accuracy. In a recently developed DNN learning software package called DeePMD-kit [20], the snapshots (which include the total potential energies, forces on each atom, and virial for a set of atomic configurations) from *ab initio* calculations are used to train interatomic potentials through DNN machine learning. After the training process, the obtained DNN model is not only able to accurately reproduce the potential energies and forces in the training data set, but also accurately predicts structural and dynamical properties of the materials being modeled. These advantages make the DNN learning method suitable for studying solidification and devitrification of alloy systems even the phase competition and transition in these systems are complex. Moreover, the

interatomic potential constructed by the trained DNN model can be ready to use in standard LAMMPS package [21] to perform MD simulations. The computational cost of the MD simulations with DNN interatomic potentials scales linearly with system size, which enables us to investigate the long-range correlations and long-time relaxations in metallic glass systems.

In this paper, development of interatomic potential for Al-rich Al-Tb Alloys by the DNN learning method is presented. In order to enhance the sampling space, the training data set for the DNN model include snapshots from pure Al and Tb liquids as well $\text{Al}_{90}\text{Tb}_{10}$ liquid at various temperature, in addition to various crystalline phases of pure Al, pure Tb, and Al-Tb binary compounds (see Table. 1). The potential energies and forces in the training data set are calculated by first-principles density functional theory (DFT) using VASP [22, 23]. We demonstrate that the obtained DNN interatomic potential from the machine learning describes accurately the structures of $\text{Al}_{90}\text{Tb}_{10}$ liquid/glass and various Al-Tb crystalline phases in comparison with those from *ab initio* calculations and experiments. Moreover, we use cluster alignment method [24] to analyze the SROs in the $\text{Al}_{90}\text{Tb}_{10}$ liquid and undercooled liquid obtained from MD simulations using the DNN potential. The results show that the Al-centered clusters are dominated by a distorted icosahedral (DISICO) motif, while the ‘3661’ and ‘15551’ motifs are the two dominant SROs for Tb-centered clusters.

The rest of paper is organized as follows. The DNN learning method for interatomic potential will be described in Sec. II. In Sec. III, we will present the details of data set generation for DNN model training and the parameters of DNN learning

process. In Sec. IV, we will demonstrate the reliability of obtained DNN interatomic potential. In Sec. V, we will use cluster alignment method to investigate the SROs development in liquid and undercooled liquid $\text{Al}_{90}\text{Tb}_{10}$ samples prepared by the MD simulations using the DNN potential. Finally, summaries and conclusions are given in Sec. VI.

II. Interatomic potential by deep neural network learning method

Artificial neural networks (NNs), inspired by the biological NNs that constitute human brain, provide an accurate tool for the representation of arbitrary functions. A NN contains interconnected layers of nodes. There are three essential types of layers: an input layer, an output layer and hidden layers (which can be multilayers depending on the complexity of the model). The input layer collects input patterns. Hidden layers perform the learning functions by adjusting the network parameters to minimize the lost function defined in the NN model. The output layer has classifications or output signals to which input patterns may map. A “node” in a NN is a mathematical function that collects and classifies information according to a specific architecture. To model the interatomic potential by NN, the information fed to the input layer is a set of descriptors $\{D_i\}$ which describe atomistic environment around every atom i of the structures in the training data set. The information extracted from the output layer are the energy E_i on each atom. Then the total potential energy E of each structure can be written as the sum of atomic energy E_i , i.e., $E = \sum_i E_i$. The mapping from the local environment of atom i (i.e., $\{D_i\}$) to energy of each atom E_i is done by the hidden layers

in the NN model where the connection weights between the nodes in different layers and the bias parameter on each node of the hidden layers are used to model this mapping [12, 19]. These weights and bias parameters are obtained by NN training which optimize the lost function with respect to the training data set. Therefore, the potential energy surface of the system is acquired once the parameters in NN have been determined by training process. Furthermore, forces on each atom can be calculated analytically from the potential energy represented by NN. A schematic illustration of artificial NNs for modeling interatomic potentials is shown in Fig. 1.

In the present study, the Potential-Smooth version of DeePMD-kit software package [19] is used to train the DNN interatomic potentials. It has demonstrated this deep learning method is very robust in developing interatomic potentials for MD simulation studies of liquid, crystalline bulk structures and organic molecules [19, 25]. A crucial step in modeling interatomic potential by DNN is the construction of local structure descriptor $\{D_i\}$ from the Cartesian coordinates of the input atomistic structures. To ensure the invariance of the total energy with respect to rotation or translation of the structures or the interchanging of two atoms of the same element in the structure, the descriptors $\{D_i\}$ have to satisfy such invariance conditions. In early work of Behler and Parrinello, a set of symmetry functions has been used for the descriptors [12]. In the present work, we adopt the local coordinate frame developed in DeePMD-kit [20] to construct the $\{D_i\}$. The description of the local environment of atom i is constructed in two steps. First, the relative Cartesian coordination $\{R_i\}$ of neighboring atoms j within cutoff radius r_c with respect to atom i are transferred to

the generalized coordination $\{\tilde{R}_i\}$ as

$$\{R_i\} = \{x_{ji}, y_{ji}, z_{ji}\} \rightarrow \{\tilde{R}_i\} = \{s(r_{ji}), \hat{x}_{ji}, \hat{y}_{ji}, \hat{z}_{ji}\} \quad (1)$$

where $\hat{x}_{ji} = s(r_{ji})x_{ji}/r_{ji}$, $\hat{y}_{ji} = s(r_{ji})y_{ji}/r_{ji}$, and $\hat{z}_{ji} = s(r_{ji})z_{ji}/r_{ji}$ have angular information of local environment. The radial information is in $s(r_{ji})$ which is smooth at the boundary of cutoff radius r_c . It is defined as [19]

$$s(r_{ji}) = \begin{cases} \frac{1}{r_{ji}}, & r_{ji} < r_{cs} \\ \frac{1}{r_{ji}} \left\{ \frac{1}{2} \cos \left[\pi \frac{r_{ji} - r_{cs}}{r_c - r_{cs}} \right] + \frac{1}{2} \right\}, & r_{cs} < r_{ji} < r_c \\ 0, & r_{ji} > r_c \end{cases} \quad (2)$$

where r_{cs} is smooth cutoff parameter. Second, an embedding neural network (called filter NN) is introduced, where the radial information $s(r_{ji})$ are fed to its input. The output of filter NN will serve as weight coefficients to the generalized coordination $\{\tilde{R}_i\}$ in constructing the local structure descriptor $\{D_i\}$ which describes the local environment of atom i . Finally, the local structure descriptor $\{D_i\}$ is fed to the input of another neural network (called fitting NN), yielding the atomic energy E_i , thus the mapping from local configuration to atomic energy is achieved.

The training process is a procedure of optimizing the parameters in filter and fitting NNs by deep learning software package such as TensorFlow [26] to minimize the total loss function. In the present work, the total loss function $L = \frac{1}{S_b} \sum_{k=1}^{S_b} L_k$ is evaluated on each training step for a subset of training data (called a batch), where S_b is the total number of snapshots in the batch. L_k is the loss function for the k th snapshot in the batch and is defined as

$$L_k = \frac{p_e}{N} |\Delta E^{(k)}|^2 + \frac{p_f}{3N} \sum_i |\Delta f_i^{(k)}|^2 \quad (3)$$

where the total potential energy error $\Delta E^{(k)}$ and force error $\Delta f_i^{(k)}$ on atom i are the

differences between the DNN predictions and *ab initio* calculation results for the atomic structure of the k th snapshot, respectively. N is total number of atoms in the structure. p_e and p_f are prefactors for energy and force respectively, which are continuously changing during the training process for optimization of DNN.

III. Training data preparation and training process

The training data set is critical to the success of the NN machine learning to generate accurate interatomic potentials for reliable MD simulations. The target of our DNN model is to simulate the liquid and glass structures of $\text{Al}_{90}\text{Tb}_{10}$ alloy. Hence, the training data set is primarily composed of the snapshots of liquid $\text{Al}_{90}\text{Tb}_{10}$ at different temperatures prepared by AIMD simulations. The AIMD simulations were performed using a cubic cell containing 180 Al atoms and 20 Tb atoms and with periodic boundary conditions. The size of unit cell is $15.989\text{\AA} \times 15.989\text{\AA} \times 15.989\text{\AA}$, which is chosen according to the density of liquid Al (n_{Al}) and liquid Tb (n_{Tb}), i.e., $n_{\text{Al}_{90}\text{Tb}_{10}} = 0.9n_{\text{Al}} + 0.1n_{\text{Tb}}$.

All the energies and forces of the structures in the training and validation data sets described below are calculated by VASP package. The time step of AIMD is taken as 3fs and NVT ensemble with Nose-Hoover thermostat [27, 28] are used in all simulations. The projector-augmented-wave (PAW) method [29] is used to describe the core-valence electron interaction. The generalized gradient approximation (GGA) in the Perdew–Burke–Ernzerhof (PBE) form [30] is used for the electronic exchange and correlation potential. The default energy cutoff for the plane wave basis set from PBE

potential is used and only the gamma point is used to sample the Brillouin zone in all AIMD simulations.

The initial configuration for the AIMD simulations was randomly selected from those generated by classical MD simulations using the available interatomic potential for Al-Sm [9]. Then the Sm atoms are replaced by Tb atoms and AIMD simulation was performed at 2000K for 2000 MD steps. Next, the sample is cooled down to 800K at a cooling rate of 3.3×10^{13} K/s. During this cooling process, snapshot atomic configurations at the temperatures of 2000K, 1800K, 1600K, 1400K, 1200K, 1100K, 1000K, 900K, 800K, respectively, are randomly picked up to initialize the isothermal MD simulations at the corresponding temperatures. The isothermal MD simulations for each temperature was performed for 90 ps and snapshots at every step of the AIMD simulations are collected. The total number of the snapshots collected for the 9 temperatures are 270,000, among them 240,000 are randomly selected as training data set and the rest of 30,000 are used as validation data set for testing the trained DNN model.

In experiment, phase separation of fcc Al has been observed in the as-quenched Al-Tb glass [31]. In order to ensure that the DNN potential can handle correctly possible phase separation, we also add snapshots of the pure Al and Tb liquids/solids into the training data set. Both the pure liquid Al (Tb) and crystal fcc Al (hcp Tb) are calculated by VASP and included in the training data set. For the pure liquid Al, the sample is simulated isothermally at $T=1400\text{K}$ and 2000K while the simulation temperatures for liquid Tb is 1800K and 2200K , respectively. Both Al and Tb liquid

sample contain 108 atoms and with periodic boundary conditions. The AIMD simulations of Al (Tb) liquid are first performed isothermally at liquid phase temperatures for 2000 steps to melt the samples and obtain the liquid state of Al (Tb). After that, all the MD steps during the following 30ps simulations for each temperature are collected. Then, in all the *ab initio* data 18,000 snapshots for Al or Tb liquids respectively are randomly picked up for the training data set. In addition, the remaining 2,000 snapshots of each pure liquids are collected for the validation data set.

The training and validation data set for our DNN learning model also included the information of the relevant crystalline phases. In order to obtain the snapshots of crystalline phases, AIMD simulations with a supercell of fcc Al (hcp Tb) containing 108 atoms at finite temperature are employed. It allows the atoms to move around the equilibrated positions in the crystals and then generate a serial snapshots of crystal structures with distortions. Moreover, in order to obtain the information about atomic structures and forces far from the equilibrium, we also carry out the *ab initio* simulations at different lattice constants. For fcc Al crystal the lattice constant is $a = 4.05(1 \pm 0.02n) \text{ \AA}$, $n = 0,1,2,3,4,5$. For hcp Tb crystal the lattice constant is $a = 3.60(1 \pm 0.02n) \text{ \AA}$, $c = 5.70(1 \pm 0.02n) \text{ \AA}$, $n = 0,1,2,3,4,5$. At each lattice constant, all atoms are distorted by means of AIMD simulations at $T=300\text{K}$. In these ways, we generate and randomly select 2,000 distorted fcc Al crystal structures and 2,000 distorted hcp Tb crystal structures at different lattice constants (or pressures) to be included in the training data set. Another 200 such distorted Al and Tb crystal structures respectively are also collected in the validation data set. In addition to the

pure Al and Tb crystalline phases, we also include the known crystalline phases of Al-Tb alloy which covered the whole composition range, i.e., $\text{Al}_{17}\text{Tb}_2$ [32], Al_4Tb [33], Al_3Tb [34], Al_2Tb [35], AlTb [36], Al_2Tb_3 [37], Al_2Tb [38] and AlTb_3 [39], to the training data set. For each of these crystalline phases, the snapshot structures were generated in the same way as that used for Al and Tb crystalline structures described above. Similarly, 2000 snapshot structures from AIMD simulations for each compound are included in the training data set and another 200 snapshots are used for the validation data set. The overall information of training and validation data set are summarized in Table 1.

In the DNN training process, in order to capture the local configuration information up to the second neighboring shell, the radial cutoff r_c is taken as 7.2 Å which is about the radial of second shell from the PPCFs in AIMD simulations of $\text{Al}_{90}\text{Tb}_{10}$ liquid. The smooth cutoff parameter r_{cs} is chosen to 7.0 Å. The filter neural network has two hidden layers with 50 and 100 nodes, respectively. The fitting neural network model has three hidden layers with equal numbers of nodes (240 nodes) per layer. The DNN is initialized with random numbers and the total number of training steps is 2,000,000. The exponentially decaying learning rate is used. At the i th training step the learning rate is defined as $r_l(i) = 0.001 \times 0.96^{i/10000}$, where the start learning rate is 0.001 and the decay rate is 0.96 with decay step of 10000. The energy prefactor p_e in loss function starts at 0.2 and ends up to 2. Meanwhile, for forces the prefactor p_f is 100 at beginning and goes down to 1 at the end of training process. The obtained interatomic potential for Al-Tb alloy in the form of DNN model (a pb file used in TensorFlow) is

provided in the Supplemental Material.

IV. Performance of the deep neural network interatomic potential

Fig. 2(a)-(d) show the comparison of energies and forces from the trained DNN model and *ab initio* results for 1,000 snapshots of $\text{Al}_{90}\text{Tb}_{10}$ liquid which are randomly picked up from the training and validation data set, respectively. The vertical coordinate represents the energies (or forces along x axis) of the snapshot structures calculated by the trained DNN model while the horizontal coordinate is the corresponding energies (or forces along x axis) obtained by *ab initio* calculations. It can be seen that the trained DNN model not only well reproduces the *ab initio* results in the training data set but also accurately predict the energies and forces for the snapshots in the validation data set. The root mean square (RMS) error of energy is below 3.0 meV/atom and the force RMS error is on the order of 0.1 eV/Å, which is sufficient for investigating the structures and dynamics of liquid. Moreover, the trained DNN model can also well predict the energies and forces for the atomic configurations which are not included in the training or validation data set. For example, although the snapshots in the AIMD simulation at temperature 1300K are not included in the training or validation data set, Fig. 2(e) and (f) show excellent prediction of energies and forces of these atomic configurations. More details of the energy and force RMS errors from the DNN model predictions for all the systems which are used to train DNN are shown Table. 1. It can be seen that the obtained DNN can well reproduce all the *ab initio* results including both liquid and crystalline structures.

The reliability and transferability of the obtained DNN potential are further tested

by using it in a MD package such as LAMMPS to study the temperature dependent structures of liquid. Fig. 3 shows the comparison of the total PPCF, Al-Al, Al-Tb, and Tb-Tb partial PPCFs of liquid $\text{Al}_{90}\text{Tb}_{10}$ at $T=1300\text{K}$ and 2000K calculated by AIMD and MD simulation with DNN potential. The initial configurations of both AIMD and MD with DNN potential is the same. The simulation times for statistical average of PPCF are 270ps and 30ps for the samples at $T=1300\text{K}$ and 2000K , respectively. It shows that the PPCFs from MD with DNN potential agree well with those from AIMD simulations, except a small discrepancy in Tb-Tb PPCFs. Such a small discrepancy would be partially attributed to the relatively poor statistics due to the small number of Tb atoms (only 20 Tb atoms compared to 180 Al atoms in a box) used in the simulation. The statistical sampling for the Tb-Tb pairs during the short MD simulation time (especially in AIMD simulation) would not be sufficient particularly at lower temperature where atoms are less mobile. When the developed DNN potential is applied to simulate the pure Al and Tb liquid, we find that the DNN potential can well reproduce the PCFs of pure Al and Tb liquid in comparison with those from AIMD, as shown in the Fig. 4. The well agreement of Tb radial distribution function as shown in Fig. 4(b) indicates that the Tb-Tb interaction predicted by DNN potential is reliable.

Besides the PPCF, the bond angle distribution can provide more structure information about the liquid samples. Thus, it can also be used to test the reliability of DNN potential. We take the first minima of PPCF as the cutoff distances to calculate the bond angle distributions and all the structures used for PPCF calculations in Fig. 3 are used to perform the statistics of bonding angles. The bond angle distributions for

$\text{Al}_{90}\text{Tb}_{10}$ liquid at $T=1300\text{K}$ and 2000K obtained in this way are shown in Fig. 5 and 6, respectively. It can be seen that the DNN potential can well reproduce the bond angle distributions from AIMD simulations.

Since glass formability strongly dependent on the competition with the nucleation and growth of various nearby crystalline phases, it is critical that the developed DNN potential can describe well the energy landscape of the Al-Tb system at the composition of interest including possible stable and metastable crystalline phases. The competition among these crystalline phases and the glass formation upon the solidification would highly correlates with their formation energies. Here the trained DNN potential is used to calculate the formation energies of crystalline phases in Al-Tb system at $T=0\text{K}$. The energies of pure fcc Al and pure hcp Tb are used as the reference for calculating the formation energy. The formation energy for crystalline phase Al_mTb_n is defined as $E_{\text{form}}(\text{Al}_m\text{Tb}_n) = [E(\text{Al}_m\text{Tb}_n) - nE(\text{Al}) - mE(\text{Tb})]/(n + m)$. Fig. 7 shows the comparison of formation energies between DNN potential and *ab initio* calculations. In both *ab initio* and DNN potential calculation, the conjugate gradient algorithm is used to optimize the atomic structures. It can be seen that the formation energies of known stable crystalline phases in training data set predicted by DNN potential agree well with the results of *ab initio* calculations. Besides the crystalline phases in the training data set, the obtained DNN potential can also well predict the formation energies of crystals that are not used for training DNN potential. For example, we calculated the formation energies of other two types of Al_3Tb crystals (the hypothetical Al_3Tb with structure of Al_3Y [40, 41] and BaPb3-type Al_3Tb founded in ref. 34). The results show that the

DNN potential reproduced the order of formation energy for all the three Al_3Tb phases. Recently, it is found that several complex metastable crystalline phases emerge in the devitrification process of $\text{Al}_{90}\text{Sm}_{10}$ system, and the structures of these complex phases have been identified by genetic algorithm (GA) search [42, 43]. These novel crystalline phases are valuable testing targets to validate the obtained DNN potential. We calculated the formation energies of $\text{Al}_{82}\text{Tb}_{10}$ (big tetra structure), $\text{Al}_{120}\text{Tb}_{22}$ (big cubic structure) and Al_5Tb (big hex structure) metastable phases in which the Al composition is close to 90%. As shown in Fig. 7, the formation energies produced by the DNN potential are all close to the values of *ab initio* calculations. All the results of formation energies and relaxed lattice parameters obtained by DNN potential and *ab initio* calculations are listed in the Table. 2.

The obtained DNN potential can be used to simulate for much larger system or much longer time compared to AIMD. Here, we have benchmarked the computation time per MD step in both AIMD and DNN MD for $\text{Al}_{90}\text{Tb}_{10}$ liquid with different system size, as shown in Fig. 8. The results show that for system containing 200 atoms (the same as the size of the liquids in the training data set) the DNN MD will be more than 3 order of magnitude faster than AIMD. In addition, the results also confirm that the computation time of DNN MD scales linear with system size. Therefore, the obtained DNN potential enable us to simulate the Al-Tb system containing up to thousands of atoms and with several tens of nanosecond simulation time.

Finally, we also perform MD simulations of Al-Tb liquid and glass using the developed DNN potential with the number of atoms much larger than those structures

in the training data set and compare the simulation results with the measurement from experiment. Experimentally, the liquid $\text{Al}_{91}\text{Tb}_9$ at 1174K was prepared by Cu-heart electric arc melting under Ar atmosphere and the glassy sample for $\text{Al}_{90}\text{Tb}_{10}$ was prepared by Cu block single melt-spinning technique, which were reported in ref. 31. The structure factors of the liquid and glass have been measured using high energy X-Ray diffraction (XRD) [31]. For comparison, our MD simulation with DNN potential of liquid $\text{Al}_{91}\text{Tb}_9$ is performed with 5000 atoms (4550 Al and 450 Tb) in a cubic box. The initial configuration is randomly picked up from the snapshots in previous MD simulation of liquid Al-Sm, where the Sm atoms are replaced by Tb atoms. First, the sample is equilibrated at 1174K for 30ps. Then MD trajectories in the subsequent simulation of 30ps at the same temperature are collected to calculate $S(q)$. Fig. 9(a) shows the calculated and experimental total structure factor of $\text{Al}_{91}\text{Tb}_9$ liquid at $T=1174\text{K}$. As one can see in Fig. 9(a), the first and second peaks of $S(q)$ from MD with DNN potential agree well with the experimental data, except that there are some deviations around the first minimum. In addition, the height of pre-peak from MD with DNN potential is higher than that of experimental data. The glass MD sample of $\text{Al}_{90}\text{Tb}_{10}$ (4500 Al and 500 Tb) at $T=300\text{K}$ is obtained by quenching from liquid of 2000K with cooling rate of 10^{11} K/s. One can see that the position and height of pre-peak from MD with DNN potential at $T=300\text{K}$ agrees well with the experimental result, as shown in Fig. 9(b). Other peak positions and heights also agree well with experimental measurement. These results show that the developed DNN potential is suitable for MD simulations of Al-rich Al-Tb liquids and glasses.

V. Short-range order in $\text{Al}_{90}\text{Tb}_{10}$ metallic liquid

Using the DNN potential developed above, we performed MD simulations to study the development of SRO in $\text{Al}_{90}\text{Tb}_{10}$ liquid as the function of temperature. The simulation is performed with 5000 atoms (4500 Al and 500 Tb) in a cubic box with periodic boundary conditions. An isothermal-isobaric ensemble and a Nose-Hoover thermostat are used in the simulation [27, 28]. The time step for simulation is 2.5fs. First the liquid $\text{Al}_{90}\text{Tb}_{10}$ sample is equilibrated at 2000K for 1 ns and then is continuously quenched down to the undercooled liquid state at $T=800\text{K}$ with the cooling rate of 10^{11} K/s. The inherent structures of liquid $\text{Al}_{90}\text{Tb}_{10}$ sample at $T=1200\text{K}$ and 950K and the undercooled sample at $T=800\text{K}$ are used to analyze the temperature dependence of the SRO in $\text{Al}_{90}\text{Tb}_{10}$.

Cluster alignment method developed previously [24] is used to analysis the SRO cluster around the Al and Tb atoms in the samples obtained from the DNN MD simulations described above. Fig. 10 shows the alignment score distributions for the Al- and Tb-centered clusters extracted from the samples at $T=1200\text{K}$, 950K , and 800K respectively against various templates as indicated in the inset of Fig. 11. Here, the alignment score is the measurement of similarity between the extracted cluster and the template. The smaller alignment score indicates the cluster and template are more similar to each other. For Al-centered clusters, we can see from Fig. 10(a)-(c) that the clusters are aligned better to the DISICO (a distorted ICO found in Ni-Zr system [45]) and ICO templates since the alignment scores with respect to these two templates have

relatively large portion of low score compared to that of the other templates. For the Tb-centered clusters, the distributions of the alignment score on the ‘3661’ and ‘15551’ templates are at the leftmost side compared to that of the other templates, as shown in Fig. 10(d)-(f). If we take 0.16 as the score cutoff value to assign the clusters to the templates, the fraction of the dominant clusters as the function of temperature can be evaluated as shown in Fig. 11. Fig. 11 (a) shows that the DISICO motif is the dominant one for the Al-centered clusters. The fraction of this type of SRO increase rapidly from about 13% at 1200K to about 31% at 800 K. For Tb-centered clusters, the ‘3661’ is the dominant SRO with its fraction increase from about 14% at 1200 K to about 40% at 800K as shown in Fig. 11 (b). The ‘15551’ SRO is also substantial, with its fraction changes from 6% to 18% when the temperature is cooled down from 1200 to 800K. We note that the ‘3661’ motif has also been identified as the dominant SRO in $\text{Al}_{90}\text{Sm}_{10}$ liquid and glass [11]. This may not be surprising due to the similarity between two rare earth elements Tb and Sm. However, the substantial ‘15551’ SRO observed in $\text{Al}_{90}\text{Tb}_{10}$ is almost absent in the $\text{Al}_{90}\text{Sm}_{10}$ liquid/glass. This would be one of the major features makes $\text{Al}_{90}\text{Tb}_{10}$ different from $\text{Al}_{90}\text{Sm}_{10}$ in phase selection and devitrification.

In order to investigate if the development of SRO in the liquid will affect the dynamics of the liquid, we use atomistic trajectories from the DNN MD simulations to investigate the dynamics of the system. To quantitatively study the dynamics properties, we calculated the self-diffusivity D which is defined as

$$D = \lim_{t \rightarrow \infty} \frac{\frac{1}{N} \langle \sum_{i=1}^N |\mathbf{R}_i(t + \tau) - \mathbf{R}_i(\tau)|^2 \rangle}{6t} \quad (4)$$

where N is the number of atoms, \mathbf{R}_i are the coordinates of atom i , the numerator is mean-square displacement (MSD), and $\langle \dots \rangle$ denotes the average over the arbitrary initial time τ . Fig. 12 shows the MSD as a function of time t for various kinds of atoms in the sample at $T=800\text{K}$. Here the cluster alignment describe above is performed on the initial atomic structure of MD trajectories to classify the atoms in the different SRO types. Then, we trace these identified atoms and calculate their MSD from the MD trajectories for 100 ps. It can be seen that the MSDs for all the atoms in the sample are proportional to simulation time. The self-diffusivity D for Al atoms is about 4 times of that for Tb atoms. Moreover, the Al and Tb atoms involved the '3661' and '15551' SRO clusters are less mobile compared to the other Al and Tb atoms which are not in '3661' or '15551' SROs. These results suggest the development of the '3661' and '15551' SRO makes the liquid becomes more sluggish and promotes the glass formation.

VI. Summary

In this paper, we have developed a DNN interatomic potential for Al-rich Al-Tb alloys by DeePMD-kit software package based on deep learning method. The VASP package is used to calculate the snapshots of liquid and crystal Al-Tb structures to prepare the training data for machine learning. In order to train a transferable model, not only liquid $\text{Al}_{90}\text{Tb}_{10}$ but also the liquid of pure Al and pure Tb, as well as the crystalline structures of Al, Tb and binary Al-Tb compounds are included in the training data set to extend the sampling space. After the training process, the obtained DNN model has been demonstrated to predict accurately the energies and forces of Al-Tb

system for both structures included and not included in the training data set.

The developed interatomic potential in the form of DNN model can be used in LAMMPS package to perform MD simulations. The results show that the DNN potential can well reproduce the PPCFs and bond angle distribution in AIMD simulations. Moreover, the calculated formation energies of crystalline phases of Al-Tb system using the DNN potential are found to be excellent agreement with *ab initio* results. Finally, the total structure factors of liquid and glass $\text{Al}_{90}\text{Tb}_{10}$ calculated by DNN potential agree well with the XRD data. In particular, the MD with DNN potential can well reproduce the positions and heights of the peaks in structure factors of $\text{Al}_{91}\text{Tb}_9$ liquid and $\text{Al}_{90}\text{Tb}_{10}$ glass as those measured in experiment. The $\text{Al}_{90}\text{Tb}_{10}$ liquid and undercooled liquid samples obtained from our simulations have also been analyzed by cluster alignment method to identify the dominant SRO structures. It is found that the Al-centered DISICO, the Tb-centered '3661' and '15551' motifs are three dominant SROs in the samples. The substantial '15551' SRO identified in $\text{Al}_{90}\text{Tb}_{10}$ sample is absent in $\text{Al}_{90}\text{Sm}_{10}$ liquid/glass, which would be a key factor for understanding the different phase selection and devitrification behaviors between $\text{Al}_{90}\text{Tb}_{10}$ and $\text{Al}_{90}\text{Sm}_{10}$.

Since the Al-RE alloys with Al-rich composition (about 90 at. % Al) is the most interesting composition range for glass formation and phase competition, our developed DNN potential is mainly trained by $\text{Al}_{90}\text{Tb}_{10}$ liquid data and the purpose of developed DNN potential is to simulate the Al-rich Al-Tb liquid. This purpose is ensured by the fact that the local composition in $\text{Al}_{90}\text{Tb}_{10}$ liquid could fluctuate around 90 at. % Al which enable the trained neural network has learned the interactions in Al-rich alloys

with different compositions around 90 at. % Al. The DNN potential has been tested for $\text{Al}_{80}\text{Tb}_{20}$ liquid at 2000 K and produced total and partial pair correlation functions in very good agreement with AIMD simulation results. Moreover, the well agreement of formation energies of crystalline phases with *ab initio* calculations shown in Fig. 7 indicates the obtained DNN has some degree of prediction power for Al-Tb crystals with different compositions. However, we have not tested the DNN potential for liquid/alloys with Al composition less than 80%. In order to develop an accurate and transferable DNN potential for Al-Tb system with all compositions, expanding the training data to include more atomic configurations with different compositions would be needed.

Acknowledgements

Work at Ames Laboratory was supported by the U.S. Department of Energy (DOE), Office of Science, Basic Energy Sciences, Materials Science and Engineering Division including a grant of computer time at the National Energy Research Supercomputing Center (NERSC) in Berkeley. Ames Laboratory is operated for the U.S. DOE by Iowa State University under contract # DE-AC02-07CH11358. L. Tang and Z. J. Yang acknowledge the support by the National Natural Science Foundation of China (Grant Nos. 11304279 and 11104247). Z. J. Yang also acknowledges the Natural Science Foundation of Zhejiang Province, China (Grant No. LY18E010007).

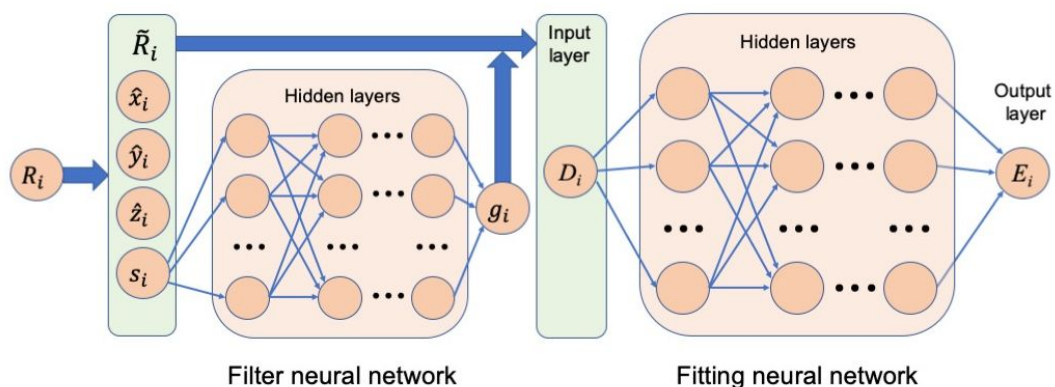


Fig. 1. The schematic illustration of deep learning method for modeling DNN interatomic potentials. First, the relative coordinates $\{R_i\}$ of neighboring atoms with respect to atoms i within cutoff radius are converted to the generalized coordinates $\{\tilde{R}_i\}$, where $\{\hat{x}_i, \hat{y}_i, \hat{z}_i\}$ have angular information and $\{s_i\}$ has radial information of local atomic environment. Second, using the radial part $\{s_i\}$ in $\{\tilde{R}_i\}$ as input, the filter NN outputs the weight coefficients $\{g_i\}$ which are added to the generalized coordination $\{\tilde{R}_i\}$. Then, the local structure descriptor $\{D_i\}$ (preserves translation, rotation and permutation symmetries) which describes the local environment of atom i is obtained. Next, $\{D_i\}$ enters into the fitting NN, yielding the atomic energy E_i which is added to the total energy E .

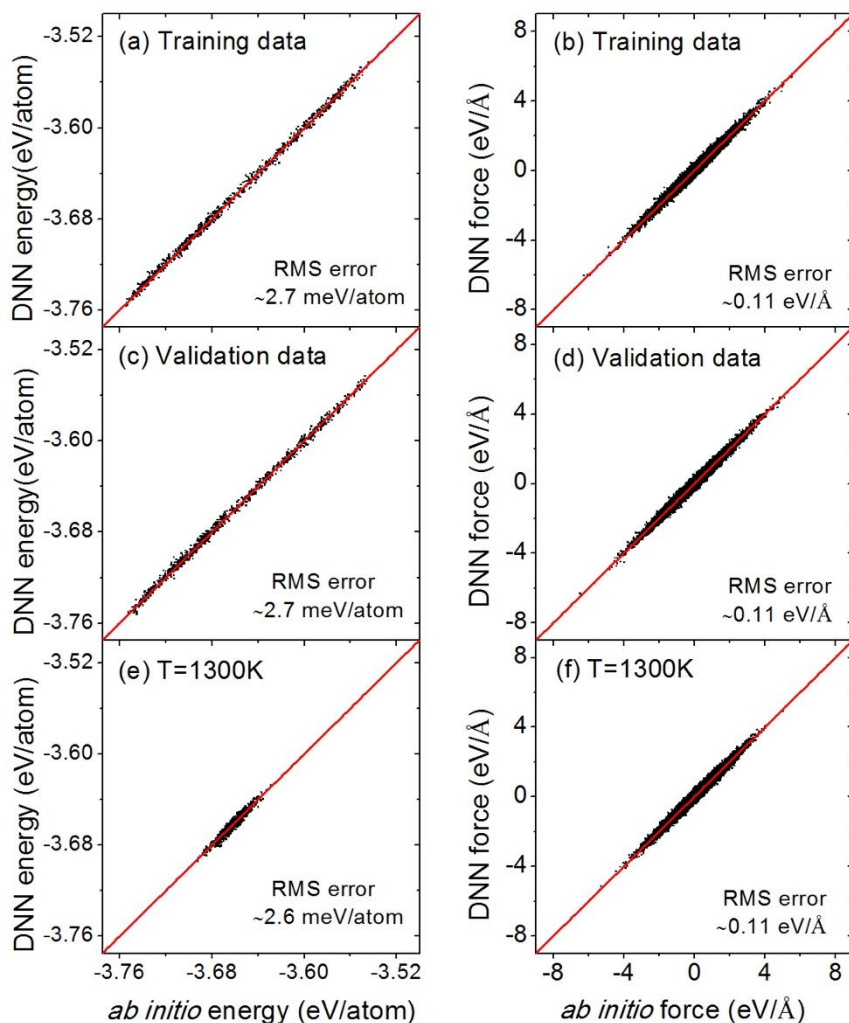


Fig. 2. Testing of energy and force predictions of the trained DNN model. Figure (a) and (b) are the comparisons of *ab initio* and DNN predicted energies and forces (along x axis) on the 1000 snapshots of $\text{Al}_{90}\text{Tb}_{10}$ liquid which are randomly picked up from the training data set. In figure (c) and (d), the 1000 snapshots in the validation data set are randomly collected. To further test the performance of DNN predictions, in figure (e) and (f) the 1000 snapshots are collected from the AIMD simulation at $T=1300\text{K}$ which is not included in the group of simulation temperatures for training or validation data set.

Systems for training DNN	Total number of atoms in box/supercell	Simulation temperatures (K)	Total simulation time (ps)	Total number of snapshots in training data set	Total number of snapshots in validation data set	Energy error (meV/atom)	Force error (eV/Å)
Al ₉₀ Tb ₁₀ liquid	200	2000, 1800, 1600, 1400, 1200, 1100, 1000, 900, 800	90 for each temperature	240,000	30,000	2.7	0.11
Tb liquid	108	1800, 2200	60	18,000	2,000	4.8	0.16
Tb crystal	108	300	6.6	2,000	200	4.4	0.09
Al liquid	108	1400, 2000	60	18,000	2,000	3.3	0.14
Al crystal	108	300	6.6	2,000	200	1.7	0.07
Al ₁₇ Tb ₂	304	300	6.6	2,000	200	3.0	0.08
Al ₄ Tb	120	300	6.6	2,000	200	1.9	0.08
Al ₃ Tb	240	300	6.6	2,000	200	1.4	0.08
Al ₂ Tb	192	300	6.6	2,000	200	1.0	0.08
AlTb	64	300	6.6	2,000	200	3.0	0.10
Al ₂ Tb ₃	160	300	6.6	2,000	200	2.1	0.09
AlTb ₂	216	300	6.6	2,000	200	2.5	0.10
AlTb ₃	108	300	6.6	2,000	200	2.8	0.09

Table 1. The overall information of training and validation data set for Al-Tb system. The RMS errors of energy and force predicted by DNN model for the validation data set of various Al-Tb system are also shown in the table.

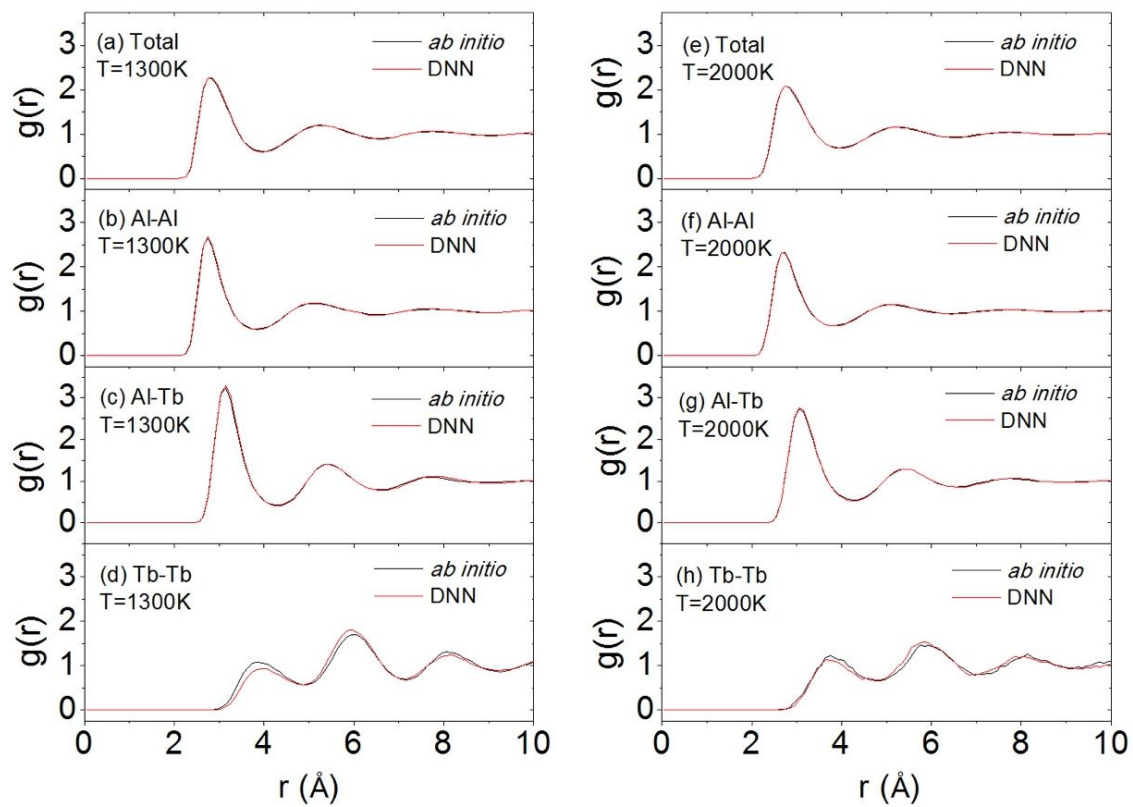


Fig. 3. Partial pair correlation functions in AIMD and MD simulations with DNN potential for liquid $\text{Al}_{90}\text{Tb}_{10}$ at (a)-(d) $T=1300\text{K}$ and (e)-(h) 2000K .

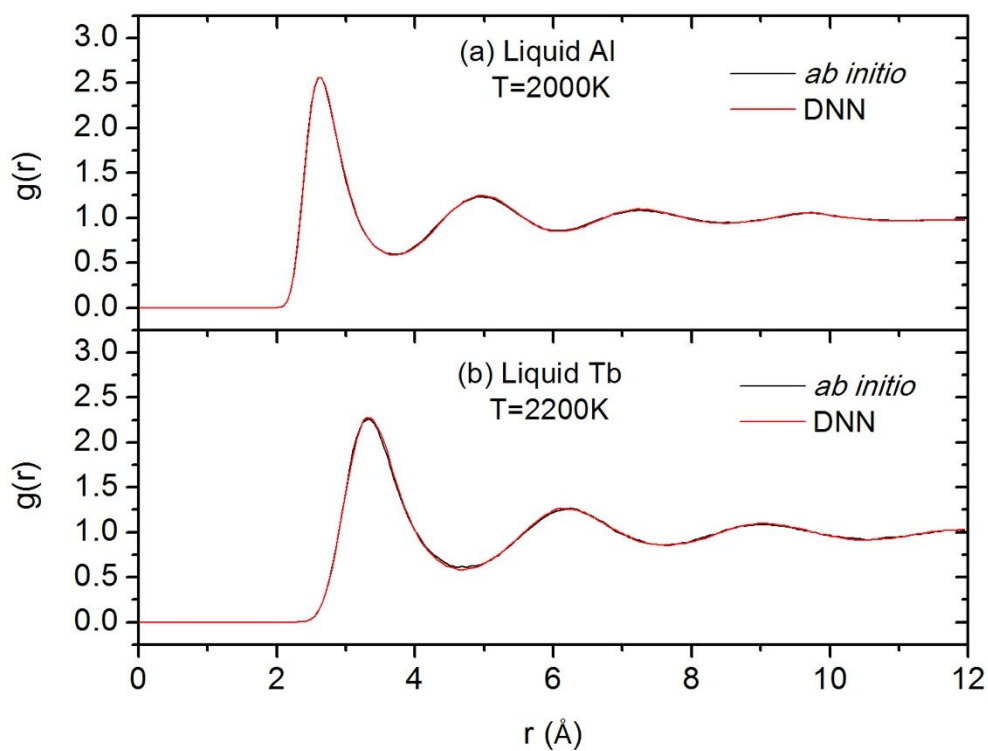


Fig. 4. Pair correlation functions in AIMD and MD simulations with DNN potential for pure liquid (a) Al and (b) Tb.

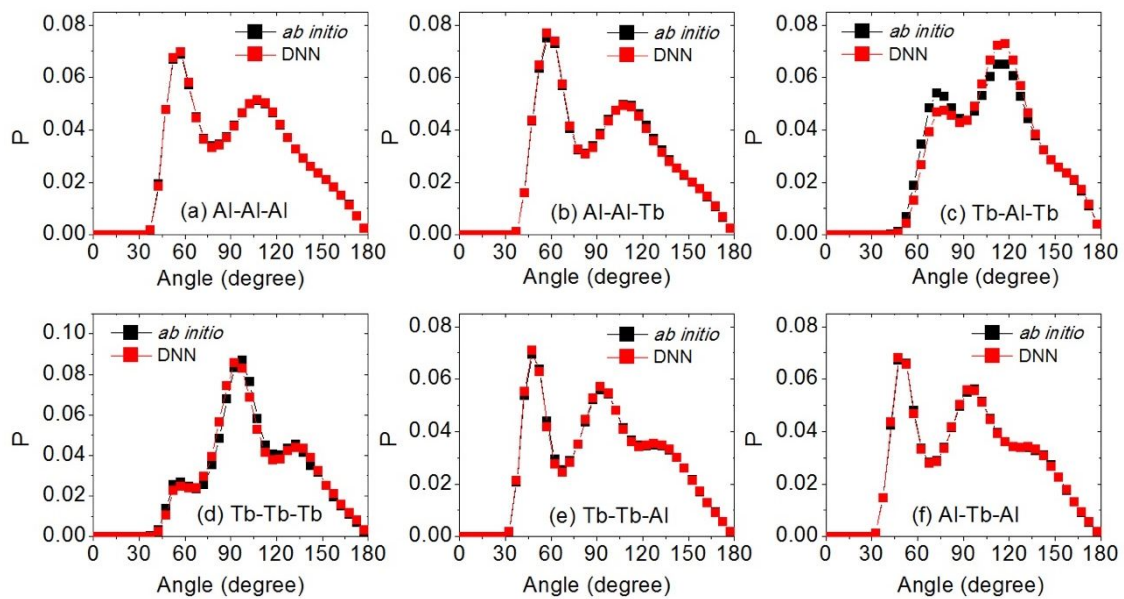


Fig. 5. The bond angle distributions in the liquid $\text{Al}_{90}\text{Tb}_{10}$ at $T=1300\text{K}$ from AIMD and MD simulations with DNN potential.

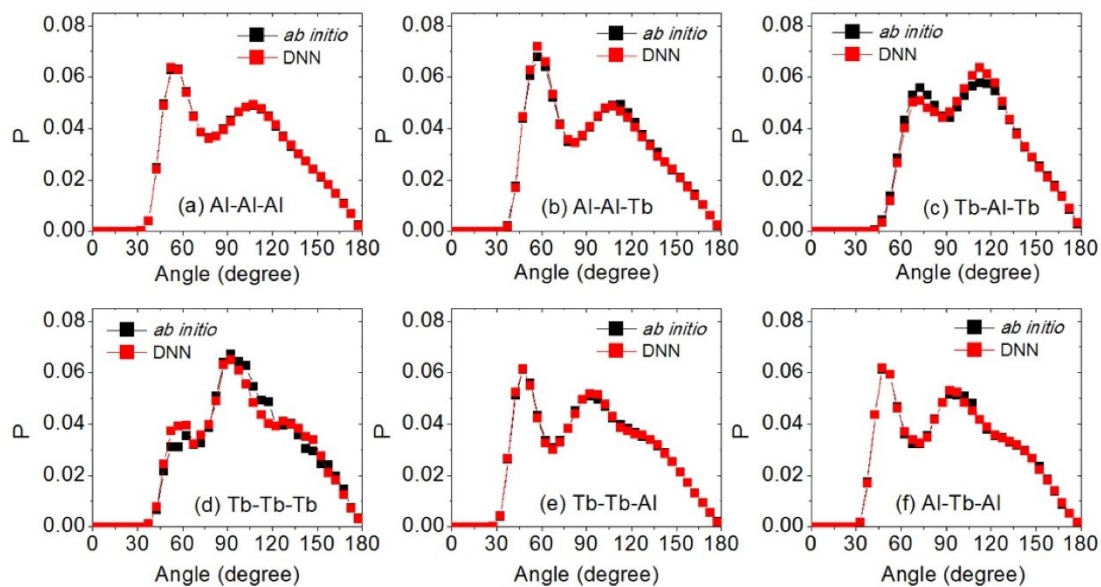


Fig. 6. The bond angle distributions in the liquid $\text{Al}_{90}\text{Tb}_{10}$ at $T=2000\text{K}$ from AIMD and MD simulations with DNN potential.

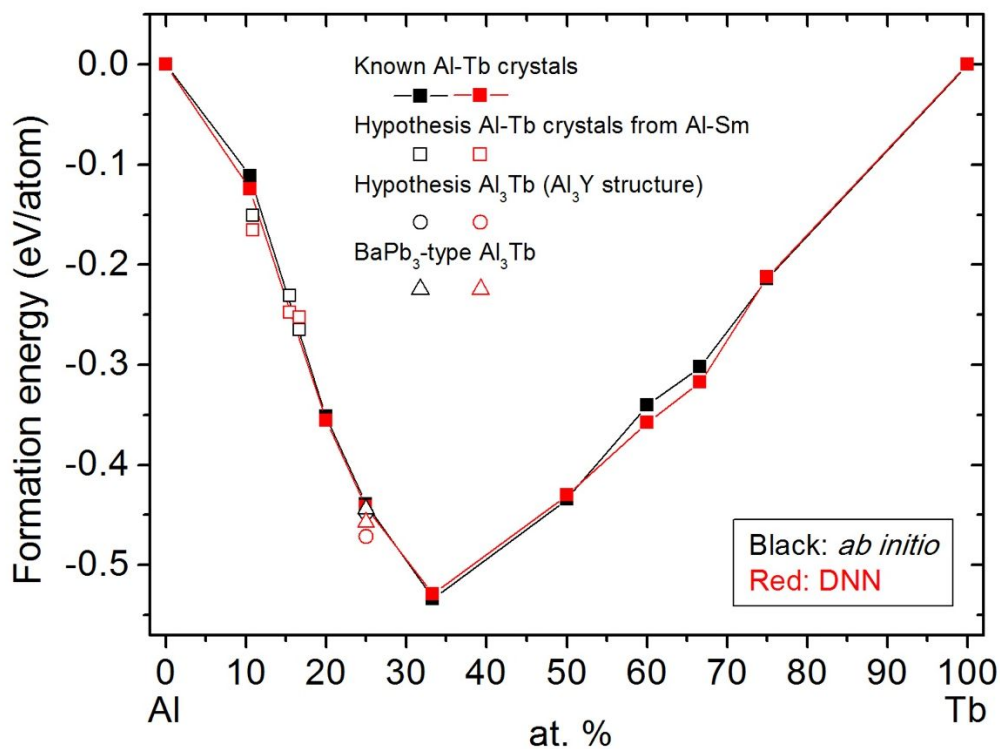
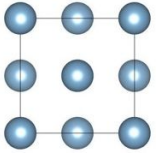
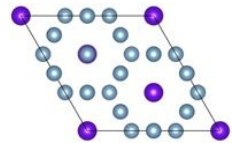
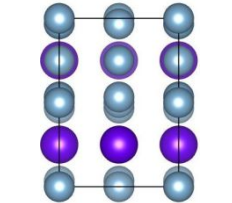
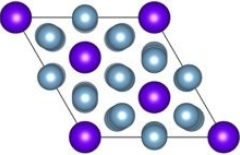
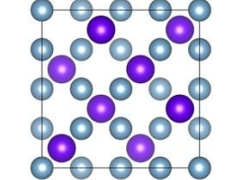
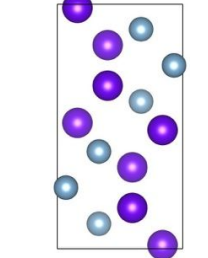
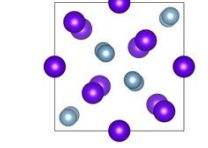
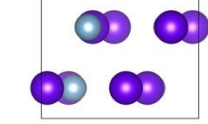


Fig. 7. The formation energies of Al-Tb system calculated by DNN potential and *ab initio* method at $T=0\text{K}$. The solid squares denote the known stable crystal structures in the training data set of Al-Tb system. The open squares denote the hypothesis Al-Tb crystal with the structures of metastable crystalline phases found in Al-Sm system. They are, from left to right, $\text{Al}_{82}\text{Tb}_{10}$ (big tetra structure), $\text{Al}_{120}\text{Tb}_{22}$ (big cubic structure), Al_5Tb (big hex structure). The open circles and triangles denote the hypothetical Al_3Tb with structure of Al_3Y and the BaPb_3 -type Al_3Tb crystal, respectively. Noted that the open data is not included in the training data set, which suggests that the obtained DNN potential has ability to predict the formation energy for the unknown Al-Tb structure around composition of 10 at. % Tb.

crystalline phase	Structure	a (Å)	b (Å)	c (Å)	α (°)	β (°)	γ (°)	Formation energy (eV/atom)
Al		4.053	4.053	4.053	90	90	90	0
		4.038	4.038	4.038	90	90	90	0
Al ₁₇ Tb ₂		9.582	9.582	8.728	90	90	120	-0.124
		9.423	9.423	9.003	90	90	120	-0.112
Al ₄ Tb		4.463	6.308	13.808	90	90	90	-0.356
		4.415	6.295	13.785	90	90	90	-0.352
Al ₃ Tb		6.110	6.110	36.049	90	90	120	-0.442
		6.130	6.130	35.985	90	90	120	-0.439
Al ₂ Tb		7.920	7.920	7.920	90	90	90	-0.529
		7.888	7.888	7.888	90	90	90	-0.534
AlTb		5.873	11.454	5.661	90	90	90	-0.430
		5.861	11.476	5.638	90	90	90	-0.434
Al ₂ Tb ₃		8.297	8.297	7.607	90	90	90	-0.358
		8.276	8.276	7.615	90	90	90	-0.341
AlTb ₂		6.597	5.117	9.447	90	90	90	-0.318
		6.575	5.037	9.640	90	90	90	-0.302

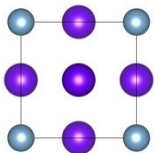
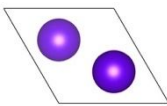
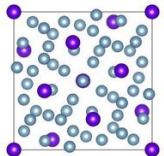
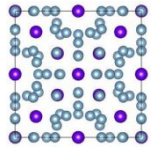
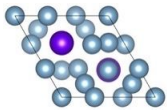
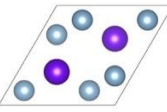
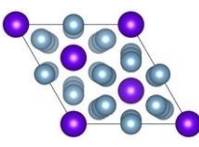
AlTb ₃		4.762	4.762	4.762	90	90	90	-0.212
		4.774	4.774	4.774	90	90	90	-0.214
Tb		3.605	3.605	5.706	90	90	120	0
		3.617	3.617	5.668	90	90	120	0
Al ₈₂ Tb ₁₀ (big tetra)		13.202	13.202	9.502	90	90	90	-0.165
		13.247	13.247	9.512	90	90	90	-0.151
Al ₁₂₀ Tb ₂₂ (big cubic)		13.781	13.781	13.781	90	90	90	-0.248
		13.822	13.822	13.822	90	90	90	-0.231
Al ₅ Tb (big hex)		5.407	5.407	17.729	90	90	120	-0.253
		5.430	5.430	17.636	90	90	120	-0.265
Al ₃ Tb (Al ₃ Y structure)		6.250	6.250	4.587	90	90	120	-0.472
		6.300	6.300	4.618	90	90	120	-0.448
BaPb ₃ -type Al ₃ Tb (from ref. 34)		6.175	6.175	21.172	90	90	120	-0.458
		6.208	6.208	21.187	90	90	120	-0.444

Table. 2. Lattice parameters and formation energies of Al-Tb crystalline phases. In calculation of the formation energy, fcc Al and hcp Tb crystal were taken as the reference states. The top value is reproduced by the DNN potential and the bottom one is calculated by the *ab initio* method.

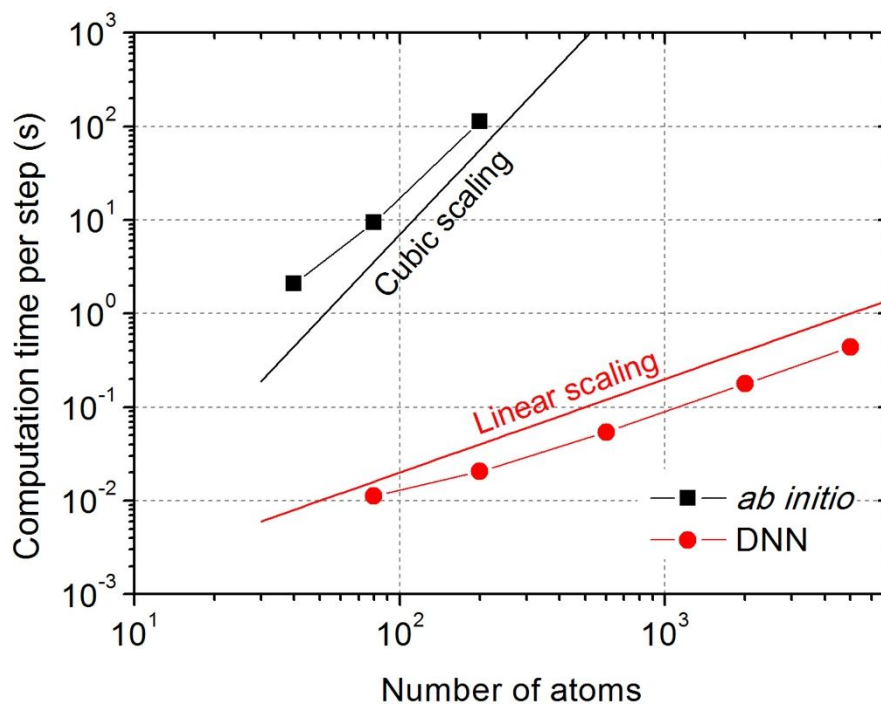


Fig. 8. The computation time per MD step calculated by *ab initio* (using ABINIT package [44]) and DNN potential versus system size. All calculations are performed on supercomputer with Intel Xeon CPU Gold 6130. It can be seen that the MD with DNN potential is linear scaling with system size. It suggests that the MD using DNN potential have ability to simulate for much larger system or much longer time compared to *ab initio*.

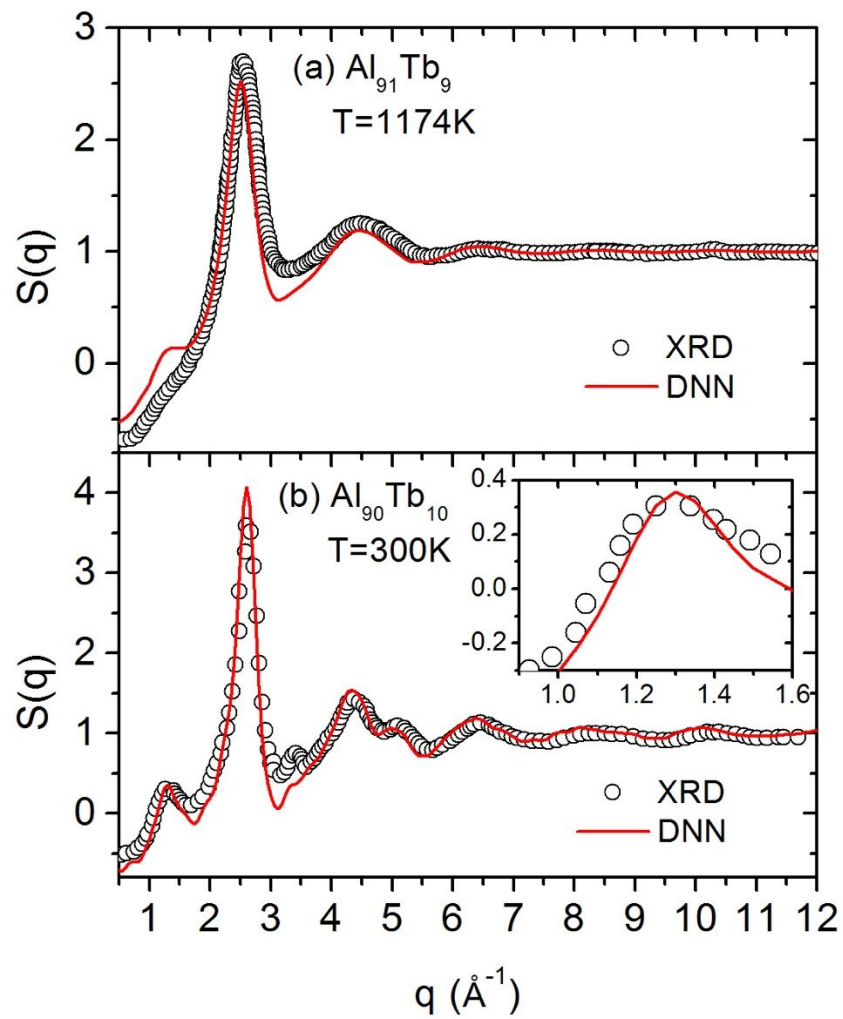


Fig. 9. The total structure factor of (a) liquid $\text{Al}_{91}\text{Tb}_9$ and (b) amorphous $\text{Al}_{90}\text{Tb}_{10}$ alloy. To obtain the amorphous $\text{Al}_{90}\text{Tb}_{10}$ for simulation, the sample is quenched from liquid at cooling rate of 10^{11} K/s. The inset figure shows the pre-peak (around 1.3\AA^{-1}) of the total structure factor. It can be seen that the MD with DNN potential well reproduces the position and height of the pre-peak.

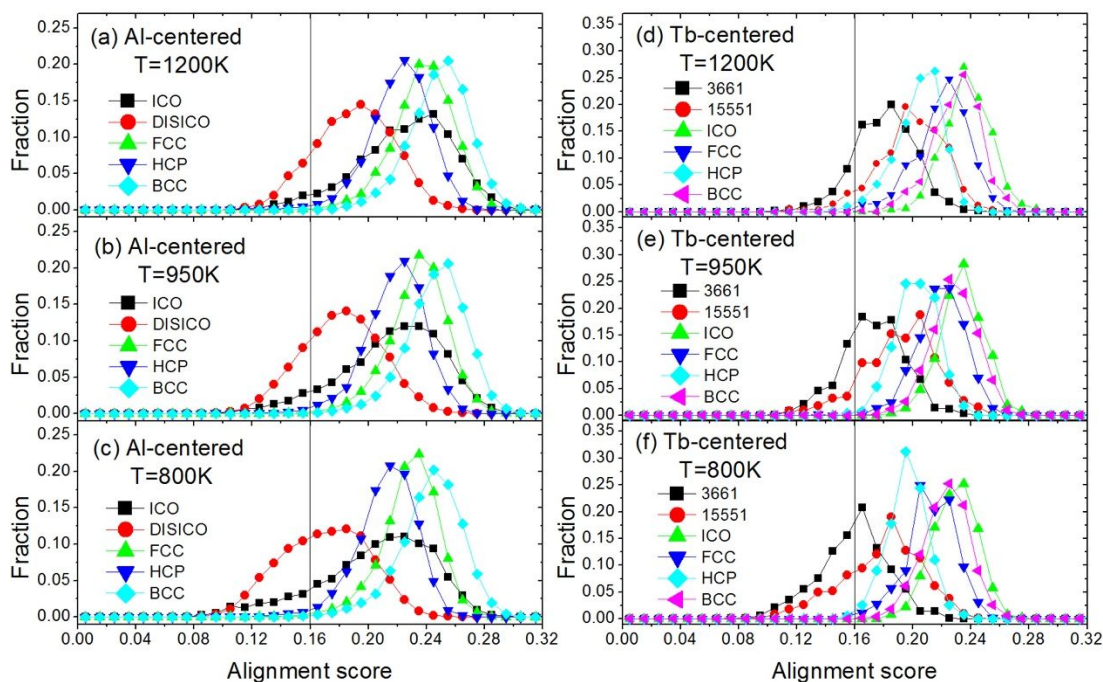


Fig. 10. The cluster alignment score distributions against various template motifs for Al- and Tb-centered clusters in the sample of 1200K, 950K, and 800K, respectively. The solid black line indicates the score cut-off value 0.16. The smaller alignment score indicates the more similar between the cluster and template motif.

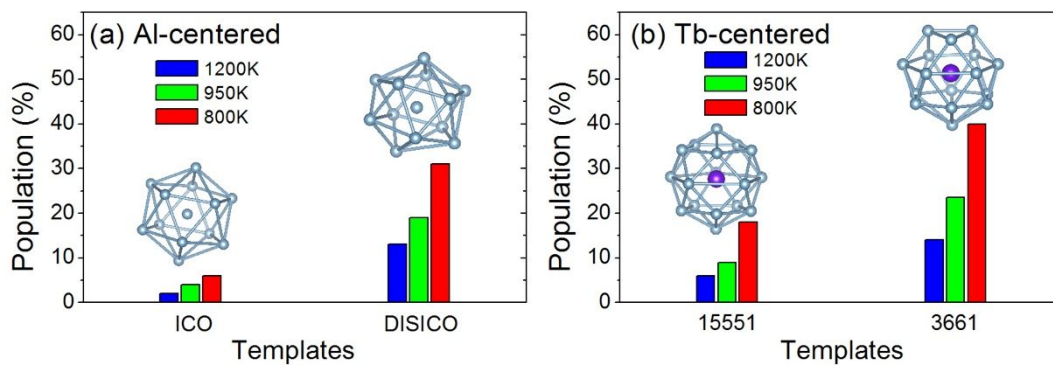


Fig. 11. The populations of Al-centered ICO, Al-centered DISICO, Tb-centered '3661', and Tb-centered '15551' clusters in the sample. At liquid state of $T=1200\text{K}$, the Tb-centered '15551' ('3661') already has considerable population. With temperature decreasing to $T=800\text{K}$, the population of the identified '3661'+ '15551' clusters in the sample increases to about 60%.

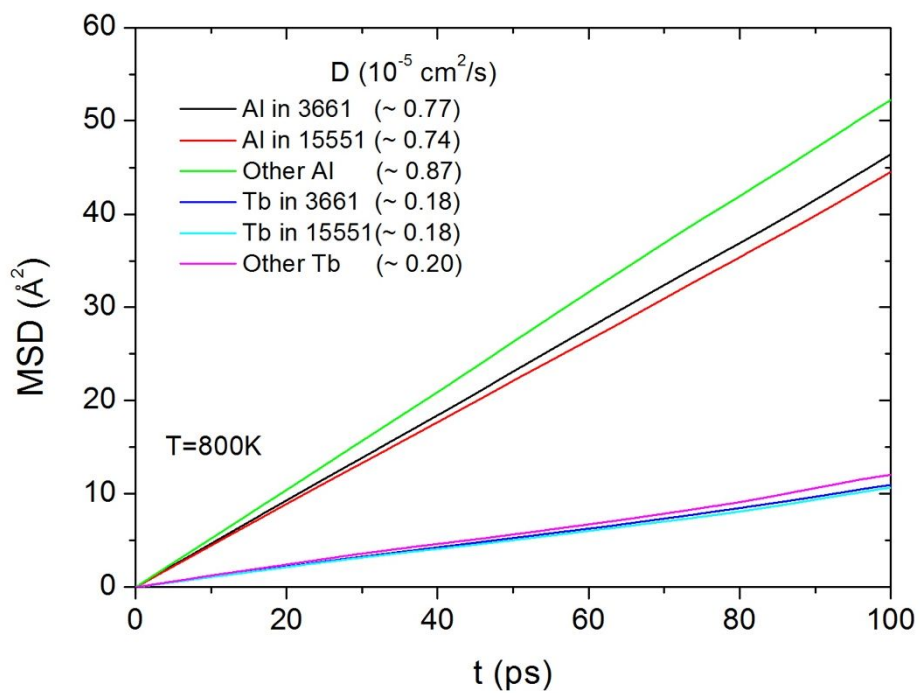


Fig. 12. The mean-square displacement of various kinds of atoms in the sample at $T=800\text{K}$, where the calculated self-diffusivities are listed in the legend.

- [1] A. Inoue, *Prog. Mater. Sci.* 43, 365 (1998).
- [2] Y. He, S. J. Poon, and G. J. Shiflet, *Science* 241, 1640 (1988).
- [3] H. S. Kim, P. J. Warren, B. Cantor, and H. R. Lee, *Nanostruct. Mater.* 11, 241 (1999).
- [4] Y. He, G. M. Dougherty, G. J. Shiflet, and S. J. Poon, *Acta Metall. Mater.* 41, 337 (1993).
- [5] A. L. Greer, *Science* 267, 1947 (1995).
- [6] J. C. Foley, D. R. Allen, and J. H. Perepezko, *Scr. Mater.* 35, 655 (1996).
- [7] Y. E. Kalay, L. S. Chumbley, and I. E. Anderson, *Mater. Sci. Eng. A* 490, 72 (2008).
- [8] A. Inoue, K. Ohtera, and T. Masumoto, *Jpn. J. Appl. Phys.* 27, L736 (1988).
- [9] M. I. Mendeleev, F. Zhang, Z. Ye, Y. Sun, M. C. Nguyen, S. R. Wilson, C. Z. Wang, and K. M. Ho, *Modelling Simul. Mater. Sci. Eng.* 23, 045013 (2015).
- [10] Feng Zhang, Yang Sun, Zhuo Ye, Yue Zhang, Cai-Zhuang Wang, Mikhail I Mendeleev, Ryan T Ott, Matthew J Kramer, Ze-Jun Ding, and Kai-Ming Ho, *J. Phys.: Condens. Matter* 27, 205701(2015).
- [11] Yang Sun, Yue Zhang, Feng Zhang, Zhuo Ye, Zejun Ding, Cai-Zhuang Wang, and Kai-Ming Ho, *J. Appl. Phys.* 120, 015901 (2016).
- [12] J. Behler and M. Parrinello, *Phys. Rev. Lett.* 98, 146401 (2007).
- [13] A. P. Bartók, M. C. Payne, R. Kondor, and G. Csányi, *Phys. Rev. Lett.* 104, 136403 (2010).
- [14] Gabriele C. Sosso, Giacomo Miceli, Sebastiano Caravati, Jörg Behler, and Marco Bernasconi, *Phys. Rev. B* 85, 174103 (2012).
- [15] A. V. Shapeev, *Multiscale Model. Simul.* 14, 1153 (2016).
- [16] S.Chmiela, A.Tkatchenko, H.E.Sauceda, I.Poltavsky, K.T. Schütt, and K.-R. Müller, *Sci. Adv.* 3, e1603015 (2017).
- [17] C. Chen, Z. Deng, R. Tran, H. Tang, I. -H. Chu, and S. P. Ong, *Phys. Rev. Mater.* 1, 043603 (2017).
- [18] Linfeng Zhang, Jiequn Han, Han Wang, Roberto Car, and Weinan E, *Phys. Rev. Lett.* 120, 143001(2018).
- [19] Linfeng Zhang, Jiequn Han, Han Wang, Wissam A. Saidi, Roberto Car, and Weinan E, arXiv:1805.09003v2
- [20] Han Wang, Linfeng Zhang, Jiequn Han, and Weinan E, *Computer Physics Communications* 228, 178 (2018).
- [21] S. Plimpton, *J. Comput. Phys.* 117, 1 (1995).
- [22] G. Kresse and J. Furthmuller, *Phys. Rev. B* 54, 11169 (1996).
- [23] G. Kresse and J. Furthmuller, *Comput. Mater. Sci.* 6, 15 (1996).
- [24] X. W. Fang, C. Z. Wang, Y. X. Yao, Z. J. Ding, and K. M. Ho, *Phys. Rev. B* 82, 184204 (2010).
- [25] Tongqi Wen, Cai-Zhuang Wang, M. J. Kramer, Yang Sun, Beilin Ye, Haidi Wang, Xueyuan Liu, Chao Zhang, Feng Zhang, Kai-Ming Ho, and Nan Wang, *Phys. Rev. B* 100, 174101 (2019).
- [26] M. Abadi, P. Barham, J. Chen, Z. Chen, A. Davis, J. Dean, M. Devin, S. Ghemawat, G. Irving, M. Isard, *et al.*, *OSDI* 16, 265 (2016).
- [27] S. Nose, *J. Chem. Phys.* 81, 511 (1984).
- [28] W. G. Hoover, *Phys. Rev. A* 31, 1695 (1985).

- [29] Vanderbilt D, *Phys. Rev. B* 41, 7892 (1990).
- [30] J. P. Perdew, K. Burke, and M. Ernzerhof, *Phys. Rev. Lett.* 77, 3865 (1996).
- [31] Y. E. Kalay, I. Kalay, Jinwoo Hwang, P. M. Voyles, M. J. Kramer, *Acta Materialia* 60, 994 (2012).
- [32] I. Pop, V. Crisan, M. Coldea, C. Hagan, and G. Borodi, *Physica B+C* 130, 504 (1985).
- [33] O. J. C. Runnalls and R. R. Boucher, *J. Less-Common Met.* 13, 431 (1967).
- [34] J. F. Cannon and H. Tracy Hall, *J. Less-Common Met.* 40, 313 (1975).
- [35] A. E. Dwight, *J. Less-Common Met.* 102, L9 (1984).
- [36] C Becla, R Lemaire, and E Parthe, *Solid State Commun.* 6, 115 (1968).
- [37] K. H. J. Buschow, *J. Less-Common Met.* 8, 209 (1965).
- [38] K. H. J. Buschow and A. S. Van Der Goot, *J. Less-Common Met.* 24, 117 (1971).
- [39] H. Haschke, H. Nowotny, and F. Benesovsky, *Monatsh. Chem.* 98, 273 (1967).
- [40] Anubhav Jain, Shyue Ping Ong, Geoffroy Hautier, Wei Chen, William Davidson Richards, Stephen Dacek, Shreyas Cholia, Dan Gunter, David Skinner, Gerbrand Ceder, and Kristin A. Persson, *APL Materials* 1, 011002 (2013).
- [41] D. M. Bailey, *Acta Cryst.* 23, 729(1967).
- [42] F. Zhang, I. McBrearty, R. T. Ott, E. Park, M. I. Mendeleev, M. J. Kramer, C. Z. Wang, and K. M. Ho, *Scr. Mater.* 81, 32 (2014).
- [43] Z. Ye, F. Zhang, Y. Sun, M. I. Mendeleev, R. T. Ott, E. Park, M. F. Besser, M. J. Kramer, Z. Ding, C.-Z. Wang, and K.-M. Ho, *Appl. Phys. Lett.* 106, 101903 (2015).
- [44] M. Torrent, F. Jollet, F. Bottin, G. Zerah, and X. Gonze, *Comput. Mat. Science* 42, 337 (2008).
- [45] Tongqi Wen, Yang Sun, Beilin Ye, Ling Tang, Zejin Yang, Kai-Ming Ho, Cai-Zhuang Wang, and Nan Wang, *J. Appl. Phys.* 123, 045108 (2018).